

# Phononic drumhead surface state in distorted kagome compound RhPb

Andrzej Ptok,<sup>1,\*</sup> William R. Meier,<sup>2,†</sup> Aksel Kobiałka,<sup>3</sup> Surajit Basak,<sup>1</sup> Małgorzata Sternik,<sup>1</sup> Jan Łażewski,<sup>1</sup> Paweł T. Jochym,<sup>1</sup> Michael A. McGuire,<sup>2</sup> Brian C. Sales,<sup>2</sup> Hu Miao,<sup>2</sup> Przemysław Piekarczyk,<sup>1</sup> and Andrzej M. Oleś<sup>4,5,‡</sup>

<sup>1</sup>*Institute of Nuclear Physics, Polish Academy of Sciences, W. E. Radzikowskiego 152, PL-31342 Kraków, Poland*

<sup>2</sup>*Material Science & Technology Division, Oak Ridge National Laboratory, Oak Ridge, Tennessee 37831, USA*

<sup>3</sup>*Department of Physics, University of Basel, Klingelbergstrasse 82, CH-4056 Basel, Switzerland*

<sup>4</sup>*Max Planck Institute for Solid State Research, Heisenbergstrasse 1, D-70569 Stuttgart, Germany*

<sup>5</sup>*Institute of Theoretical Physics, Jagiellonian University, Profesora Stanisława Łojasiewicza 11, PL-30348 Kraków, Poland*

(Dated: September 6, 2023)

RhPb was initially recognized as one of a CoSn-like compounds with  $P6/mmm$  symmetry, containing an ideal kagome lattice of  $d$ -block atoms. However, theoretical calculations predict the realization of the phonon soft mode which leads to the kagome lattice distortion and stabilization of the structure with  $P\bar{6}2m$  symmetry [A. Ptok *et al.*, *Phys. Rev. B* **104**, 054305 (2021)]. Here, we present the single crystal x-ray diffraction results supporting this prediction. Furthermore, we discuss the main dynamical properties of RhPb with  $P\bar{6}2m$  symmetry. The bulk phononic dispersion curves contain several flattened bands, Dirac nodal lines, and triple degenerate Dirac points. As a consequence, the phononic drumhead surface state is realized for the (100) surface, terminated by the zigzag-like edge of Pb honeycomb sublattice.

## I. INTRODUCTION

Discovery of the topological insulators with conducting surface states in the form of the Dirac cone [1–4] opened a period of the intensive studies in the subject of fermionic topological systems [5–7]. However, a realization of the non-trivial topological states is not limited only to fermionic systems but can be also expected in bosonic ones as well [8–12]. We can find several examples of the realization of phonon Dirac/Weyl points [13–27], nodal lines [28–33], nodal rings [33–38], and nodal nets [39–42]. Topological properties are also manifested by the emergence of phonon surface states [15–19, 32, 35, 36, 43–49] or phonon Hall effect [50–56]. As a result, existence of the topological phonons with non-zero Berry curvature [57] can give rise to development of nanodevices based on the heat transfer manipulation, i.e., in *phononics* [58].

In the context of the topological properties, the kagome-supported systems have been of great interest recently. The basic property of the system with the kagome lattice is the formation of flat electronic bands [59–61]. One such example of the kagome system are CoSn-like compounds, which combine kagome and honeycomb layers [62–65]. The electronic band structure exhibits a flat band and Dirac fermions [62–70]. Some CoSn-like compounds exhibit frustrated magnetism with an important role for itinerant electrons [71], like magnetically ordered FeGe [72], or FeSn [62, 70, 73, 74]. However, most commonly, these compounds are paramagnets, such as CoSn [73].

*Motivation:* Typically kagome layer in CoSn-like compounds crystallizes with the  $P6/mmm$  symmetry [62, 63]. In such a structure, the  $d$ -block element (e.g. Fe, Co, Ni, Rh, or Pt) forms an ideal kagome sublattice, while the  $p$ -block element (e.g. Ge, In, Sn, Tl, or Pb) has two non-equivalent positions: one of the  $p$ -block elements is located in the plane of the kagome sublattice when the second's position forms honeycomb sublattice intercalated between two kagome-sublattice planes. RhPb satisfies the mentioned conditions, and therefore it should behave as an ideal kagome metal [63]. However, theoretical investigations of the lattice dynamics of RhPb show that this compound should be unstable with  $P6/mmm$  symmetry [75]. Stabilization of RhPb can be achieved by distorting the kagome lattice, resulting in  $P\bar{6}2m$  symmetry (see Fig. 1). In this paper, we present experimental evidence for the distorted kagome structure in the RhPb system. Furthermore, we investigate the dynamic properties of RhPb with distorted kagome lattice. We show that this compound is an excellent candidate

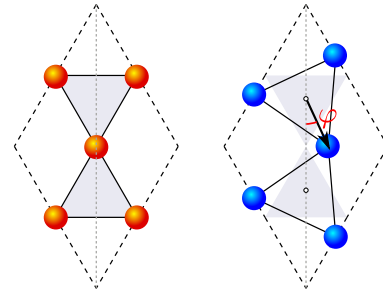


FIG. 1. Schematic representation of the *ideal* (left panel) and *distorted* (right panel) kagome lattices, realized in the system with symmetries  $P6/mmm$  and  $P\bar{6}2m$ , respectively. In the ideal kagome lattice, the system is centrosymmetric. The rotation of perfectly ordered triangles by angle  $\varphi$  transforms the system into the non-centrosymmetric structure.

\* e-mail: [aptok@mmj.pl](mailto:aptok@mmj.pl)

† e-mail: [javamochoam@gmail.com](mailto:javamochoam@gmail.com); Current address: Materials Science & Engineering Department, University of Tennessee Knoxville, Knoxville, Tennessee 37996, USA

‡ e-mail: [a.m.oles@fkf.mpg.de](mailto:a.m.oles@fkf.mpg.de)

for the study of the phonon drumhead surface state.

The paper is organized as follows. Firstly, we discuss the results indicating formation of the distorted kagome lattice in RhPb with  $P\bar{6}2m$  symmetry (Sec. II). Next, we discuss the theoretical study of the dynamical properties of this compound (Sec. III). Finally, we summarize the paper with the main conclusions in Sec. IV.

## II. CRYSTAL STRUCTURE

Crystals of RhPb were grown from a high-temperature Pb-rich melt [63]. A 1:3 atomic ratio of rhodium sponge (Alfa Aesar 99.95%) and lead slugs (Alfa Aesar Pura-tronic 99.999%) were loaded into one side of 2 mL alumina Canfield crucible set [76] and then sealed in a fused silica ampoule under vacuum with a hydrogen-oxygen torch. The ampoule was placed in a box furnace and heated to 1000°C or 1100°C over 6 h. This temperature was held for 2 hours to dissolve the rhodium in lead and homogenize the fluid. The furnace was quickly cooled to 900°C over 3.5 h and held for 0.5 h before cooling to 750°C over 320 h ( $-0.47^\circ\text{C}/\text{h}$ ) to slowly precipitate the crystal. The hot ampoule was removed from the furnace and inverted into a centrifuge to fling the remaining liquid of the crystals. In the batch used for single crystal diffraction, 5.4 g of reactants yielded a single  $4 \times 7$  mm crystals weighing about 1.2 g. It had a slightly-skeletal hexagonal-prismatic shape with a shiny metallic luster [see Fig. 2(a)]. Other batches of crystals yielded faceted euhedral blocky hexagonal prisms. Crystals of RhPb are brittle with a conchoidal fracture and have weak (001)-cleavage. Broken surfaces sometimes reveal inclusions of bluish metallic Pb metal that contrast with the silver metallic RhPb surfaces.

To determine the crystal structure of RhPb, fragments of the 1.2 g crystal were selected for single crystal X-ray diffraction (XRD). The crystal, approximately  $60 \times 40 \times 10 \mu\text{m}^3$ , was mounted on the end of a Kapton loop with Loctite glue for data collection at room temperature using a Bruker D8 Quest diffractometer (0.71073 Å Mo Ka radiation). Data were collected, reduced, and analyzed using APEX3 software, including a semi-empirical absorption correction based on equivalent reflections. Structure refinement was performed using

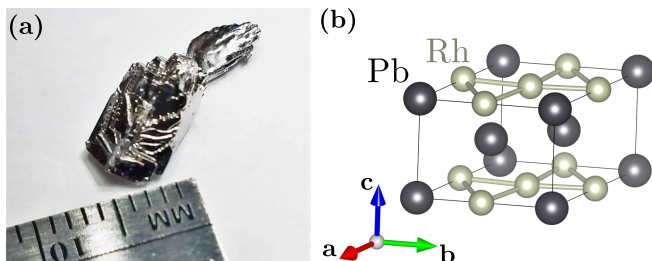


FIG. 2. Single crystal of RhPb grown from lead melt (a), and crystal structure of RhPb with  $P\bar{6}2m$  symmetry (b).

TABLE I. An important characteristic of refined structures of RhPb at 293 K from single crystal x-ray diffraction. Note the significant improvement of fit quality in the  $P\bar{6}2m$  refinement.

Space Group	$P6/mmm$	$P\bar{6}2m$
$x_{\text{Rh}}$	1/2	0.4775(2)
Twin fraction	N/A	0.568(25)
Triangle rotation, $\varphi$ in Fig. 1	$0^\circ$	$4.45(3)^\circ$
R(obs) (%)	6.01	2.83
Goodness of fit obs	4.91	1.65

JANA 2020 [77] for both  $P6/mmm$  (space group No. 191) and  $P\bar{6}2m$  (space group No. 189) symmetries.

The first-principles density functional theory (DFT) calculations were performed using the projector augmented-wave (PAW) potentials [78] implemented in the Vienna Ab initio Simulation Package (VASP) code [79–81]. Calculations were made within the generalized gradient approximation (GGA) in the Perdew, Burke, and Ernzerhof (PBE) parameterization [82]. The energy cutoff for the plane-wave expansion was set to 350 eV. Optimizations of structural parameters (lattice constants and atomic positions) are performed in the primitive unit cell using the  $10 \times 10 \times 6$   $\mathbf{k}$ -point grid in the Monkhorst–Pack scheme [83]. As a break condition of the optimization loop, we take the energy difference of  $10^{-6}$  eV and  $10^{-8}$  eV for ionic and electronic degrees of freedom, respectively.

*Structure:* Initially, the RhPb structure was assumed to be possess  $P6/mmm$  symmetry [63]. However, theoretical analysis of the RhPb dynamical properties show that such a system is unstable [75]. Our single crystal refinement do indeed reveal that RhPb adopts the distorted  $P\bar{6}2m$  structure based on a distinctly better fit quality over the  $P6/mmm$  solution (Tab. I). DFT calculations estimate very subtle differences in the lattice parameters for the two structures (Tab. II) but more stable phonons in the  $P\bar{6}2m$  structure (detailed discussion in Sec. III A).

In the case of  $P6/mmm$  symmetry, the Rh atoms are located in the Wyckoff position  $3f$  ( $1/2, 1/2, 0$ ), while the Pb atoms in two non-equivalent Wyckoff positions  $2d$  ( $1/3, 2/3, 1/2$ ) and  $1a$  ( $0, 0, 0$ ). In the case of the  $P\bar{6}2m$  symmetry [see Fig. 2(b)], the  $3f$  position of the Rh atom is calculated to lie at  $(0.467, 0.467, 0)$ . Experimentally, the position of the Rh atom was estimated as

TABLE II. Comparison of the experimental and theoretical lattice constants for RhPb with different symmetries.

	$a$ (Å)	$c$ (Å)
Exp. 293(2) K	5.6794(4)	4.4311(3)
Exp. 15 K (Ref. [63])	5.66601(2)	4.41267(1)
$P6/mmm$	5.740	4.487
$P\bar{6}2m$	5.762	4.466

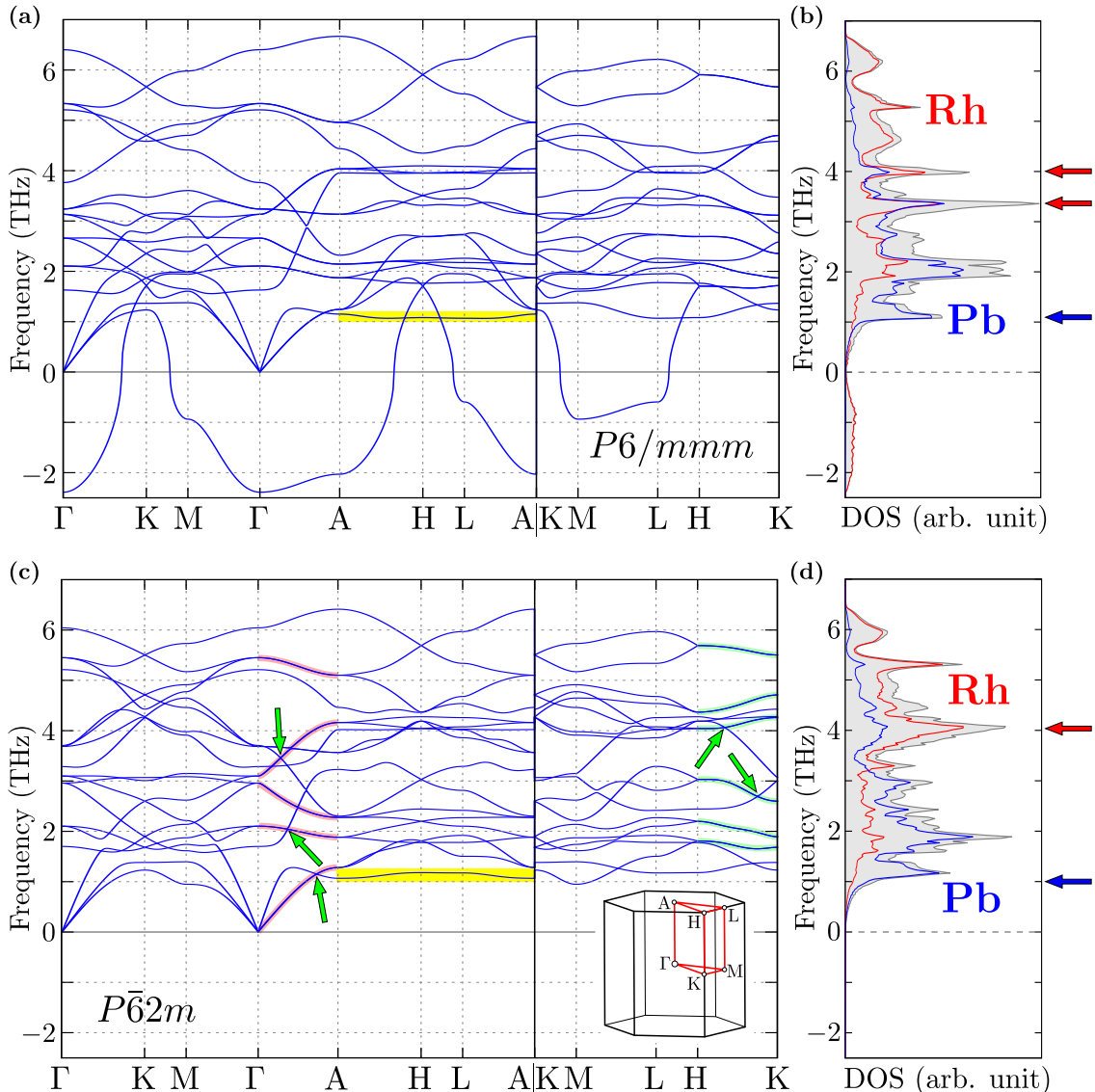


FIG. 3. Phonon dispersion relations (left column) and phonon density of states (right column) for RhPb with  $P6/mmm$  (top row) and  $P62m$  (bottom row) symmetry. The marked red and green branches correspond to the double degenerate band along the  $\Gamma$ -A and K-H directions, respectively. Color lines in the right panels are related to the total DOS (gray) or partial DOS (red and blue for lighter Rh and heavier Pb atoms, respectively). The inset in panel (c) represents the Brillouin zone and its high symmetry points.

$(0.4775(2), 0.4775(2), 0)$ . The distortion introduced to the system corresponds to the rotation of the triangles that form an ideal kagome lattice with angle  $\varphi = 6.5^\circ$  determined by DFT, while the experimentally obtained value is  $4.46^\circ$  (see Fig. 1). The rotation of the kagome triangles in RhPb mirrors the modified kagome pattern seen in the ZrNiAl-type materials [84–92]. More crystallographic data (e.g. CIF files as well as XRD refinements) can be found in the Supplemental Material (SM) [93].

Regardless of the symmetry, RhPb exhibits a metallic band structure (see Fig. S1 in SM [93]). The electronic band structure obtained for both symmetries is very similar, and in correspondence to other CoSn-like

compounds, it contains several flattened bands (detailed discussion can be found in Sec. S1 in the SM [93]).

### III. DYNAMICAL PROPERTIES

The dynamical properties were calculated using the direct *Parlinski-Li-Kawazoe* method [94], implemented in PHONOPY package [95]. Within this method, the interatomic force constants (IFC) are calculated from the Hellmann-Feynman (HF) forces acting on the atoms after displacements of individual atoms inside the supercell. We performed these calculations using the  $2 \times 2 \times 2$  su-

percell with 48 atoms, and the reduced  $\mathbf{k}$ -grid  $3 \times 3 \times 3$ . Next, the IFC were used to study the surface states, by calculations of the surface Green's function for semi-infinite system [96], by WANNIERTOOLS [97]. Additionally, we also calculate the phonon dispersion curves for a finite temperature. In this case, the calculations were performed for the thermal distribution of multi-displacement of atoms [98], generated within the HECSS procedure [99]. The total energy and HF forces acting on all atoms are calculated with VASP for 100 different configurations of atomic displacements in the supercell. In dynamical properties calculations, we include second- and third-order phonon contributions, which correspond to the harmonic and cubic IFC, respectively.

### A. Phonon dispersion curves

The phonon dispersion relations and the phonon density of states (DOS) for RhPb with both symmetries are presented in Fig. 3. In the case of the  $P6/mmm$  symmetry, there exists the imaginary soft mode (presented as negative frequencies) [see Fig. 3(a)]. This soft mode, with frequency of  $-2.59$  THz at the  $\Gamma$  point, is characterized by the  $B_{1u}$  symmetry. Atomic displacements induced by this mode lead to the rotation of the triangles forming the ideal kagome lattice [75] (see Fig. 1). As a consequence, the  $P\bar{6}2m$  symmetry is stabilized – after the transformation the phonon dispersion does not exhibit any imaginary modes, so all frequencies are positive [Fig. 3(c)]. The analysis of the zone-center mode frequencies and symmetries shows that in the distorted structure the mode corresponding to the soft-mode has a frequency of 3.2 THz and an  $A$ -like symmetry.

Soft modes realized for the  $P6/mmm$  symmetry are associated only with the Rh atoms vibration, which is reflected in the phonon density of states. In practice, all spectral weights at DOS related to the soft mode [negative frequencies at Fig. 3(b)] correspond to the Rh atoms contribution. For negative frequencies the contribution of Pb atoms is negligible. Indeed, stabilization of RhPb with the  $P\bar{6}2m$  symmetry modified mainly the Rh contribution [cf. Fig. 3(b) and 3(d)]. As expected, independently of the system symmetry, the vibrations of the heavy Pb atoms are realized mostly in the lower frequencies range. The vibrations of lighter Rh atoms exist in the higher frequency range.

Here, we should point out that the spontaneous kagome rotation can be also achieved in other compounds, like e.g.  $\text{MgCo}_6\text{Ge}_6$  [100] at  $T = 100$  K. Nevertheless, in the case of RhPb, the theoretical investigation of temperature-dependent phonon dispersion for  $P6/mmm$  always shows soft mode at the  $\Gamma$  point (even up to 1500 K). From this, we can conclude that the RhPb compound crystallizes only with the  $P\bar{6}2m$  symmetry, while the structure with the  $P6/mmm$  symmetry is unstable even at high temperatures.

Symmetry realized by RhPb has an impact on the irre-

ducible representation of phonons at the  $\Gamma$  point. Indeed, the exact analysis presented in the Sec. S2 in SM [93] clearly shows differences between these two phases. In fact, due to the different number of active modes in both symmetries, e.g. visible in the Raman spectroscopy, we can gain additional evidence for the formation of the  $P\bar{6}2m$  crystal symmetry.

### B. Phonon flat bands

Typically, the kagome lattice allows for the realization of the flat bands – this property is observed in the electronic band structure of CoSn-like compounds [63–66]. However, similar behavior is also observed in phonon dispersion curves. For both symmetries, there are several flat bands with a weak dispersion along the  $\Gamma$ –K–M– $\Gamma$  and A–H–L–A paths [e.g. branch marked by yellow areas in Figs. 3(a) and 3(c)]. A previous study of the similar CoSn system, suggests that the flat bands at low frequencies should be related with the collective vibrations of  $d$ -block atoms (i.e., Rh in our case) within the (ideal or distorted) kagome lattice [101]. However, exact analysis of the phonon DOS clearly shows that these modes are related to the vibrations of Pb atoms [marked by blue arrows in Figs. 3(b) and 3(d)]. Additionally, at this range of frequencies, the chiral phonons (i.e., circulations of the atoms around the equilibrium position) were predicted within the Pb honeycomb sublattice [75].

The realization of mentioned flat bands is reflected in the phonon DOS, by the relatively sharp peaks [marked by red arrows in Figs. 3(b) and 3(d)]. Moreover, the phonon DOS describes the frequency distribution of normal modes inside the whole Brillouin zone, in contrast to the phonon dispersion curves which only represent the modes along high symmetry directions. Indeed, the true flat-like bands can be realized in  $P6/mmm$  symmetry, where the peaks in DOS are very sharp [see Fig. 3(b)]. Contrary to this, in the case of  $P\bar{6}2m$  symmetry, the stronger  $\mathbf{k}$ -dependent dispersion is uncovered

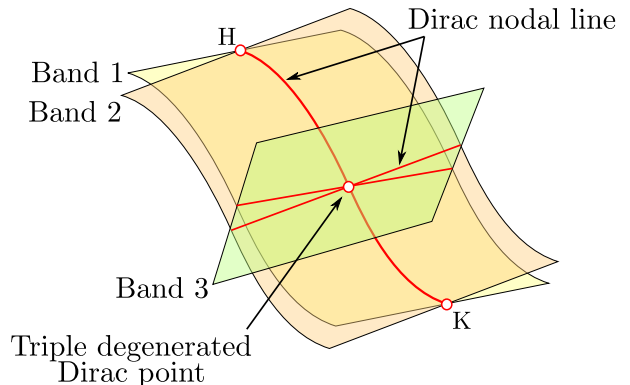


FIG. 4. Schematic representation of triple degenerated Dirac point forming along the K–H path.

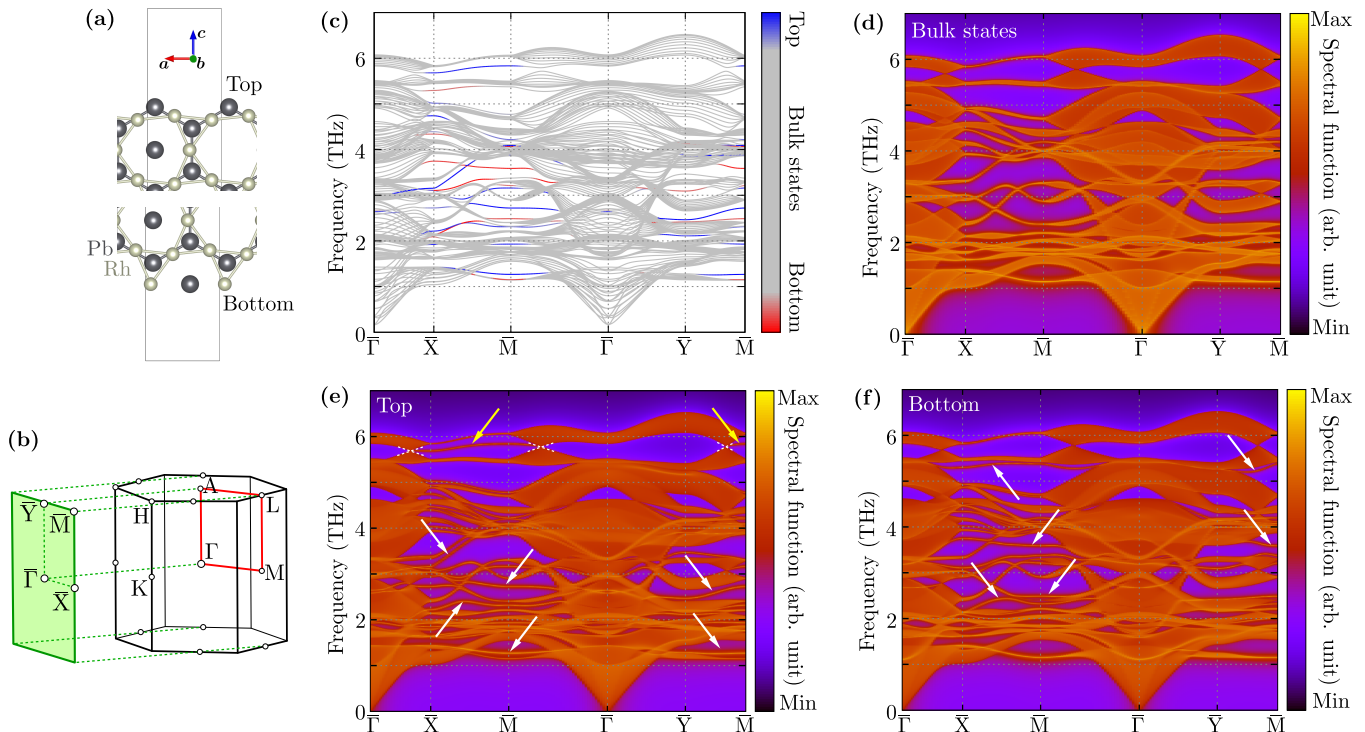


FIG. 5. The phonon surface states realized at the edge of the (100) surfaces of RhPb with  $P\bar{6}2m$  symmetry are presented in (a). For simplification, we show only bonding between Rh atoms forming a distorted kagome lattice and Pb atoms forming a honeycomb lattice. The Pb atom in the center of hexagons is placed in the plane of a distorted kagome lattice. (b) Relation between the bulk (3D) and surface (2D) Brillouin zone. Phonon band structure calculated for slab-like structure (c), containing ten layers. The colors correspond to the states related to vibrations of the atoms at the top surface (blue), central bulk-like part (gray), or bottom surface (red). The panels from (d) to (f) present the spectral function calculated for the central bulk-like part, the top surface, and the bottom surface part of the slab, respectively. The arrows in (e) and (f) show the locations of the soft modes of the phonons realized on the top or bottom surfaces, respectively.

by the existence of much broader peaks in phonon DOS [see Fig. 3(d)]. It means, that the phonon bands for the  $P\bar{6}2m$  symmetry are more dispersive than in the case of the  $P6/mmm$  symmetry.

### C. Bands degeneracy and Dirac points/lines

The realization of three- and six-folded rotational symmetry allows preserving band degeneracy from  $\Gamma$  points. Indeed, the degeneracy preservation is well visible along the  $\Gamma$ -A path (i.e., for  $z$  direction, perpendicular to the honeycomb and kagome layers) [branches marked by the red solid line in Fig 3(c)]. Additionally, the hexagonal symmetry affects the band structure along the K-H path, where some bands are double-degenerated and form the Dirac nodal lines. Irreducible representations at the K (H) point allow for the realization of double degenerated points with the  $K_5$  and  $K_6$  ( $H_5$  and  $H_6$ ) symmetry. However, the symmetry of this state is preserved for any point P with coordinates  $(1/3, 1/3, u)$ , within the double degenerated state with the  $P_3$  symmetry. Finally, the Dirac point at the K (H) point [visible e.g. in the form of characteristic band crossing around 5.6 THz for both

symmetries in Fig. 3(a) and (c)], is “stretched” out along all the K-H path forming the Dirac line.

Additionally, in the phonon dispersion curves a few crossings of the bands with different degeneracy along the  $\Gamma$ -Z and along the K-H directions can be found [places shown by green arrows in Fig. 3(c)]. This type of crossing forms the Dirac point with tripled degeneracy [see Fig. 4]. In this case, two bands (No. 1 and 2) are crossing along the K-H path, as discussed in the previous paragraph. Additional band (no. 3) crosses initial two bands creating additional Dirac nodal lines (by crossing one of them), and triple degenerated Dirac point (in places of crossing both bands simultaneously). Here we would like to point out that the realization of (bulk) Dirac point and nodal lines has a strong effect on possible surface states. Indeed, in the next paragraph, we will focus on this aspect.

### D. Phonon surface states

Some hexagonal lattices, like honeycomb [102–104] and kagome [105, 106] nets, can form the electronic surface states at the zigzag-like edge of the lattice. This is also

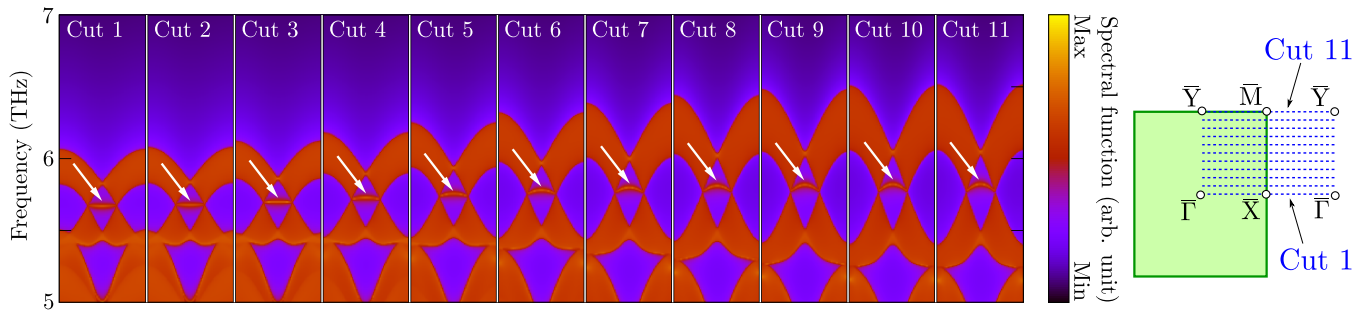


FIG. 6. The surface spectral function for different cuts of the surface (2D) Brillouin zone (right panel), presenting  $\mathbf{k}$ -dependence of the phonon drumhead surface state (marked by white arrows).

true in the case of the bosonic systems [43, 107–110]. Indeed, the phonon zigzag edge modes could be realized in RhPb at the (100) surface [Fig. 5(a)]. Similar behavior was also earlier reported for NbReSi, which possesses the same symmetry [111].

The calculation of the phonon surface states of RhPb for the (100) surface is presented in Fig. 5. In our calculations, we consider two types of terminations. The zigzag edge of the Pb honeycomb lattice is realized in both of them. The “top” surface contains also a chain of Rh atoms from the kagome lattice. Similarly, the “bottom” surface contains a chain of Rh-Pb atoms from the triangular lattice formed by the Rh kagome net decorated by Pb atoms represented by non-bonded black atom in Fig. 5(a). Slab-like calculations (for ten layers of RhPb) clearly show the existence of surface states, independently of the termination [blue and red lines in Fig. 5(c)]. The phonon dispersion curves in this case contain much more branches than the dispersion curves for the bulk [Fig. 3(c)], what is the consequence of projection of all phonon states from the bulk (3D) Brillouin zone onto the 2D Brillouin zone of the surface [see Fig. 5(b)]. It is interesting that, in the case of the surface directly terminated by the zigzag edge of the Pb honeycomb lattice (i.e., top surface), the phonon surface states at the highest frequencies exhibit behavior similar to this observed in electronic surface states at the zigzag edge in graphene nanoribbon [102] [see the states with frequencies around 5.75 THz, marked by yellow arrows in Fig. 5(e)].

Direct calculations of the spectral functions for the bulk and surface regions are presented in Figs. 5(d)–5(f). The phonon surface states can be in a relatively simple way extracted from the bulk spectra, by comparing the spectral function related to the bulk states [see Fig. 5(d)] with the adequate spectral function for a specific surface [Fig. 5(e) or 5(f)]. Additional states, i.e., surface states, are marked by arrows. Comparing the frequencies of surface states with the bulk phonon DOS [Fig. 3(d)], we see that the surface states in the low (high) frequency range should be realized mostly by Pb (Rh) atoms.

Probably, the most interesting properties of the slab-like structure can be observed for the highest branches of the spectrum. First, the signature of the bulk Dirac

“point” [i.e., Dirac lines from the K-H direction in the 3D bulk Brillouin zone are projected on the 2D surface Brillouin zone, see Fig. 5(b)] can be well recognized in the spectrum [white dashed crosses in Fig. 5(e)]. Between these points, the mentioned earlier zigzag-like edge mode is formed.

However, a more precise analysis of this latter state uncovers the realization of the drumhead phononic surface state. Indeed, as we can recognize in Fig. 6, these surface state is realized independently of  $\mathbf{k}$ , forming 2D surface state between the two bulk Dirac lines mentioned earlier. Formation of the drumhead phonon surface state is presented schematically in Fig. 7. Remarkably, the projected bulk phonon surface state create a graphene-like spectrum, independently of  $\mathbf{k}$ . Note that the band crossing discussed earlier (red line in Fig. 7) is visible as a Dirac “point” for any  $\mathbf{k}$ . Finally, the drumhead surface state are realized between the Dirac nodal lines. Curiously, the frequency of phonon drumhead surface state strongly depends on  $\mathbf{k}$  (Fig. 6).

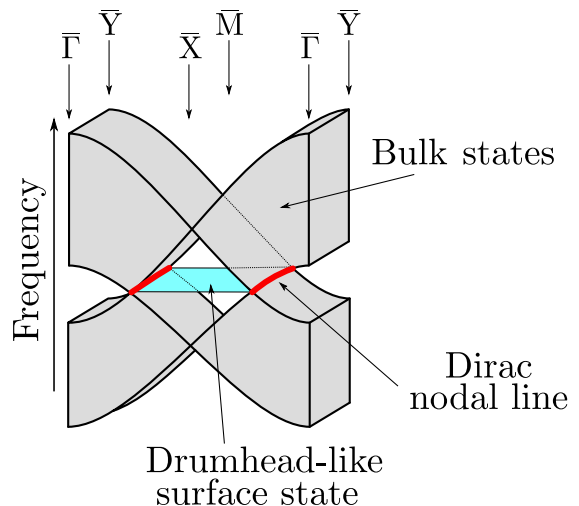


FIG. 7. Schematic representation of the forming of phonon drumhead surface state.

#### IV. SUMMARY

In this paper we discuss the basic properties of RhPb with the distorted kagome lattice of Rh atoms. Initially presented theoretical calculations [75], predict the realization of the distorted kagome lattice in RhPb. Indeed, our single crystal diffraction results confirm the predicted distortion of the kagome net in RhPb.

We presented a study of the dynamical properties of the bulk RhPb compound. In such a system, the emergence of several flattened phonon bands is possible. However, a more precise analysis shows that phonons in this band have even broader dispersion than for an ideal kagome lattice. This behavior is clearly seen in the phonon density of states.

The phonon dispersion curves exhibit several interesting features, namely the (bulk) Dirac nodal lines and triple degenerated Dirac points. Such structures have consequences for the observed surface states. The most prominent example is the realization of phonon drum-head surface state, between two (bulk) Dirac nodal lines

projected on the surface Brillouin zone. In this context, the RhPb crystal with the distorted kagome lattice is an excellent platform to study the interplay between topological phonon surface states and electronic flat bands.

#### ACKNOWLEDGMENTS

We kindly thank Mark O. Goerbig for insightful discussions. Some figures in this work were rendered using VESTA [112] and XCRYSDEN [113] software. A.P. is grateful to Laboratoire de Physique des Solides in Orsay (CNRS, University Paris Saclay) for hospitality during a part of the work on this project. Work by W.R.M., M.A.M, B.C.S., and H.M. was funded by the U.S. Department of Energy, Office of Science, Basic Energy Sciences, Materials Sciences and Engineering Division. A.M.O. is grateful for support via the Alexander von Humboldt Foundation Fellowship (Humboldt-Forschungspreis). We kindly acknowledge support by National Science Centre (NCN, Poland) under Project No. 2021/43/B/ST3/02166.

- 
- [1] H. Zhang, C.-X. Liu, X.-L. Qi, X. Dai, Z. Fang, and S.-C. Zhang, Topological insulators in  $\text{Bi}_2\text{Se}_3$ ,  $\text{Bi}_2\text{Te}_3$  and  $\text{Sb}_2\text{Te}_3$  with a single Dirac cone on the surface, *Nat. Phys.* **5**, 438 (2009).
  - [2] Y. Xia, D. Qian, D. Hsieh, L. Wray, A. Pal, H. Lin, A. Bansil, D. Grauer, Y. S. Hor, R. J. Cava, and M. Z. Hasan, Observation of a large-gap topological-insulator class with a single Dirac cone on the surface, *Nat. Phys.* **5**, 398 (2009).
  - [3] D. Hsieh, Y. Xia, D. Qian, L. Wray, F. Meier, J. H. Dil, J. Osterwalder, L. Patthey, A. V. Fedorov, H. Lin, A. Bansil, D. Grauer, Y. S. Hor, R. J. Cava, and M. Z. Hasan, Observation of time-reversal-protected single-Dirac-cone topological-insulator states in  $\text{Bi}_2\text{Te}_3$  and  $\text{Sb}_2\text{Te}_3$ , *Phys. Rev. Lett.* **103**, 146401 (2009).
  - [4] Z. Alpichshev, J. G. Analytis, J.-H. Chu, I. R. Fisher, Y. L. Chen, Z. X. Shen, A. Fang, and A. Kapitulnik, STM imaging of electronic waves on the surface of  $\text{Bi}_2\text{Te}_3$ : Topologically protected surface states and hexagonal warping effects, *Phys. Rev. Lett.* **104**, 016401 (2010).
  - [5] M. Z. Hasan and C. L. Kane, Colloquium: Topological insulators, *Rev. Mod. Phys.* **82**, 3045 (2010).
  - [6] X.-L. Qi and S.-C. Zhang, Topological insulators and superconductors, *Rev. Mod. Phys.* **83**, 1057 (2011).
  - [7] N. P. Armitage, E. J. Mele, and A. Vishwanath, Weyl and Dirac semimetals in three-dimensional solids, *Rev. Mod. Phys.* **90**, 015001 (2018).
  - [8] L. Lu, J. D. Joannopoulos, and M. Soljačić, Topological photonics, *Nature Photonics* **8**, 821 (2014).
  - [9] Z. Yang, F. Gao, X. Shi, X. Lin, Z. Gao, Y. Chong, and B. Zhang, Topological acoustics, *Phys. Rev. Lett.* **114**, 114301 (2015).
  - [10] T. Ozawa, H. M. Price, A. Amo, N. Goldman, M. Hafezi, L. Lu, M. C. Rechtsman, D. Schuster, J. Simon, O. Zilberberg, and I. Carusotto, Topological photonics, *Rev. Mod. Phys.* **91**, 015006 (2019).
  - [11] Y. Liu, X. Chen, and Y. Xu, Topological phononics: From fundamental models to real materials, *Adv. Funct. Mater.* **30**, 1904784 (2020).
  - [12] P. A. McClarty, Topological magnons: A review, *Annu. Rev. Condens. Matter Phys.* **13**, 171 (2022).
  - [13] H. Miao, T. T. Zhang, L. Wang, D. Meyers, A. H. Said, Y. L. Wang, Y. G. Shi, H. M. Weng, Z. Fang, and M. P. M. Dean, Observation of double Weyl phonons in parity-breaking FeSi, *Phys. Rev. Lett.* **121**, 035302 (2018).
  - [14] J. Li, Q. Xie, J. Liu, R. Li, M. Liu, L. Wang, D. Li, Y. Li, and X.-Q. Chen, Phononic Weyl nodal straight lines in  $\text{MgB}_2$ , *Phys. Rev. B* **101**, 024301 (2020).
  - [15] J. Li, Q. Xie, S. Ullah, R. Li, H. Ma, D. Li, Y. Li, and X.-Q. Chen, Coexistent three-component and two-component Weyl phonons in TiS, ZrSe, and HfTe, *Phys. Rev. B* **97**, 054305 (2018).
  - [16] R. Wang, B. W. Xia, Z. J. Chen, B. B. Zheng, Y. J. Zhao, and H. Xu, Symmetry-protected topological triangular Weyl complex, *Phys. Rev. Lett.* **124**, 105303 (2020).
  - [17] Z. J. Chen, R. Wang, B. W. Xia, B. B. Zheng, Y. J. Jin, Y.-J. Zhao, and H. Xu, Three-dimensional Dirac phonons with inversion symmetry, *Phys. Rev. Lett.* **126**, 185301 (2021).
  - [18] T. Zhang, Z. Song, A. Alexandradinata, H. Weng, C. Fang, L. Lu, and Z. Fang, Double-Weyl phonons in transition-metal monosilicides, *Phys. Rev. Lett.* **120**, 016401 (2018).
  - [19] M. Zhong, Y. Liu, F. Zhou, M. Kuang, T. Yang, X. Wang, and G. Zhang, Coexistence of phononic sixfold, fourfold, and threefold excitations in the ternary antimonide  $\text{Zr}_3\text{Ni}_3\text{Sb}_4$ , *Phys. Rev. B* **104**, 085118 (2021).

- [20] C. Xie, Y. Liu, Z. Zhang, F. Zhou, T. Yang, M. Kuang, X. Wang, and G. Zhang, Sixfold degenerate nodal-point phonons: Symmetry analysis and materials realization, *Phys. Rev. B* **104**, 045148 (2021).
- [21] P.-F. Liu, J. Li, X.-H. Tu, H. Li, J. Zhang, P. Zhang, Q. Gao, and B.-T. Wang, First-principles prediction of ideal type-II Weyl phonons in wurtzite ZnSe, *Phys. Rev. B* **103**, 094306 (2021).
- [22] J. Liu, W. Hou, E. Wang, S. Zhang, J.-T. Sun, and S. Meng, Ideal type-II Weyl phonons in wurtzite CuI, *Phys. Rev. B* **100**, 081204(R) (2019).
- [23] Q.-B. Liu, Y. Qian, H.-H. Fu, and Z. Wang, Symmetry-enforced Weyl phonons, *npj Comput. Mater.* **6**, 95 (2020).
- [24] Q.-B. Liu, Z. Wang, and H.-H. Fu, Charge-four Weyl phonons, *Phys. Rev. B* **103**, L161303 (2021).
- [25] J. Wang, H. Yuan, Y. Liu, F. Zhou, X. Wang, and G. Zhang, Hourglass Weyl and Dirac nodal line phonons, and drumhead-like and torus phonon surface states in orthorhombic-type KCuS, *Phys. Chem. Chem. Phys.* **24**, 2752 (2022).
- [26] G. Ding, J. Wang, Z.-M. Yu, Z. Zhang, W. Wang, and X. Wang, Single pair of type-III Weyl points half-metals: BaNiO<sub>6</sub> as an example, *Phys. Rev. Mater.* **7**, 014202 (2023).
- [27] Y. Yang, C. Xie, Y. Cui, X. Wang, and W. Wu, Maximally charged single-pair multi-Weyl point phonons in *P23*-type BeH<sub>2</sub>, *Phys. Rev. B* **107**, 054310 (2023).
- [28] X. Wang, T. Yang, Z. Cheng, G. Surucu, J. Wang, F. Zhou, Z. Zhang, and G. Zhang, Topological nodal line phonons: Recent advances in materials realization, *Appl. Phys. Rev.* **9**, 041304 (2022).
- [29] G. Liu, Y. Jin, Z. Chen, and H. Xu, Symmetry-enforced straight nodal-line phonons, *Phys. Rev. B* **104**, 024304 (2021).
- [30] C. Xie, H. Yuan, Y. Liu, X. Wang, and G. Zhang, Three-nodal surface phonons in solid-state materials: Theory and material realization, *Phys. Rev. B* **104**, 134303 (2021).
- [31] M. Wang, Y. Wang, Z. Yang, J. Fan, B. Zheng, R. Wang, and X. Wu, Symmetry-enforced nodal cage phonons in Th<sub>2</sub>BC<sub>2</sub>, *Phys. Rev. B* **105**, 174309 (2022).
- [32] S. Basak, A. Kobialka, and A. Ptok, Dynamical properties of *T*<sub>3</sub>Pb<sub>2</sub>Ch<sub>2</sub> (*T* = Pd, Pt and *Ch* = S, Se) with transition metal kagome net, *Adv. Phys. Research* **2**, 2300025 (2023).
- [33] F. Zhou, Z. Zhang, H. Chen, M. Kuang, T. Yang, and X. Wang, Hybrid-type nodal ring phonons and coexistence of higher-order quadratic nodal line phonons in an AgZr alloy, *Phys. Rev. B* **104**, 174108 (2021).
- [34] B. Zheng, B. Xia, R. Wang, Z. Chen, J. Zhao, Y. Zhao, and H. Xu, Ideal type-III nodal-ring phonons, *Phys. Rev. B* **101**, 100303(R) (2020).
- [35] Y. J. Jin, Z. J. Chen, B. W. Xia, Y. J. Zhao, R. Wang, and H. Xu, Ideal intersecting nodal-ring phonons in bcc Cs, *Phys. Rev. B* **98**, 220103(R) (2018).
- [36] B. Zheng, F. Zhan, X. Wu, R. Wang, and J. Fan, Hourglass phonons jointly protected by symmorphic and non-symmorphic symmetries, *Phys. Rev. B* **104**, L060301 (2021).
- [37] R. Y. Wang, Z. J. Chen, Z. Q. Huang, B. W. Xia, and H. Xu, Classification and materials realization of topologically robust nodal ring phonons, *Phys. Rev. Mater.* **5**, 084202 (2021).
- [38] Z. J. Chen, Z. J. Xie, Y. J. Jin, G. Liu, and H. Xu, Hybrid nodal-ring phonons with hourglass dispersion in AgAlO<sub>2</sub>, *Phys. Rev. Mater.* **6**, 034202 (2022).
- [39] Y. S. Chen, F. F. Huang, P. Zhou, Z. S. Ma, and L. Z. Sun, Ideal topological phononic nodal chain in K<sub>2</sub>O materials class, *New J. Phys.* **23**, 103043 (2021).
- [40] F. Zhou, H. Chen, Z.-M. Yu, Z. Zhang, and X. Wang, Realistic cesium fluogermanate: An ideal platform to realize the topologically nodal-box and nodal-chain phonons, *Phys. Rev. B* **104**, 214310 (2021).
- [41] G. Ding, T. Sun, and X. Wang, Ideal nodal-net, nodal-chain, and nodal-cage phonons in some realistic materials, *Phys. Chem. Chem. Phys.* **24**, 11175 (2022).
- [42] J. Zhu, W. Wu, J. Zhao, H. Chen, L. Zhang, and S. A. Yang, Symmetry-enforced nodal chain phonons, *npj Quantum Mater.* **7**, 52 (2022).
- [43] J. Li, L. Wang, J. Liu, R. Li, Z. Zhang, and X.-Q. Chen, Topological phonons in graphene, *Phys. Rev. B* **101**, 081403(R) (2020).
- [44] J. Wang, H. Yuan, Z.-M. Yu, Z. Zhang, and X. Wang, Coexistence of symmetry-enforced phononic Dirac nodal-line net and three-nodal surfaces phonons in solid-state materials: Theory and materials realization, *Phys. Rev. Mater.* **5**, 124203 (2021).
- [45] Q.-B. Liu, Z.-Q. Wang, and H.-H. Fu, Ideal topological nodal-surface phonons in RbTeAu-family materials, *Phys. Rev. B* **104**, L041405 (2021).
- [46] J. Wang, H. Yuan, M. Kuang, T. Yang, Z.-M. Yu, Z. Zhang, and X. Wang, Coexistence of zero-, one-, and two-dimensional degeneracy in tetragonal SnO<sub>2</sub> phonons, *Phys. Rev. B* **104**, L041107 (2021).
- [47] Q.-B. Liu, H.-H. Fu, and R. Wu, Topological phononic nodal hexahedron net and nodal links in the high-pressure phase of the semiconductor CuCl, *Phys. Rev. B* **104**, 045409 (2021).
- [48] Z. Wang, W. Zhou, A. N. Rudenko, and S. Yuan, Lattice dynamics and topological surface phonon states in cuprous oxide Cu<sub>2</sub>O, *Phys. Rev. B* **103**, 195137 (2021).
- [49] Y. Yang, J. Wang, Y. Liu, Y. Cui, G. Ding, and X. Wang, Topological phonons in Cs-Te binary systems, *Phys. Rev. B* **107**, 024304 (2023).
- [50] C. Strohm, G. L. J. A. Rikken, and P. Wyder, Phenomenological evidence for the phonon Hall effect, *Phys. Rev. Lett.* **95**, 155901 (2005).
- [51] L. Sheng, D. N. Sheng, and C. S. Ting, Theory of the phonon Hall effect in paramagnetic dielectrics, *Phys. Rev. Lett.* **96**, 155901 (2006).
- [52] Y. Kagan and L. A. Maksimov, Anomalous Hall effect for the phonon heat conductivity in paramagnetic dielectrics, *Phys. Rev. Lett.* **100**, 145902 (2008).
- [53] L. Zhang, J. Ren, J.-S. Wang, and B. Li, Topological nature of the phonon Hall effect, *Phys. Rev. Lett.* **105**, 225901 (2010).
- [54] T. Qin, J. Zhou, and J. Shi, Berry curvature and the phonon Hall effect, *Phys. Rev. B* **86**, 104305 (2012).
- [55] T. Saito, K. Misaki, H. Ishizuka, and N. Nagaosa, Berry phase of phonons and thermal Hall effect in nonmagnetic insulators, *Phys. Rev. Lett.* **123**, 255901 (2019).
- [56] X. Zhang, Y. Zhang, S. Okamoto, and D. Xiao, Thermal Hall effect induced by magnon-phonon interactions, *Phys. Rev. Lett.* **123**, 167202 (2019).
- [57] L. Zhang and Q. Niu, Chiral phonons at high-symmetry points in monolayer hexagonal lattices, *Phys. Rev. Lett.* **115**, 115502 (2015).

- [58] N. Li, J. Ren, L. Wang, G. Zhang, P. Hänggi, and B. Li, Colloquium: Phononics: Manipulating heat flow with electronic analogs and beyond, *Rev. Mod. Phys.* **84**, 1045 (2012).
- [59] Z. Lin, J.-H. Choi, Q. Zhang, W. Qin, S. Yi, P. Wang, L. Li, Y. Wang, H. Zhang, Z. Sun, L. Wei, S. Zhang, T. Guo, Q. Lu, J.-H. Cho, C. Zeng, and Z. Zhang, Flat-bands and emergent ferromagnetic ordering in  $\text{Fe}_3\text{Sn}_2$  kagome lattices, *Phys. Rev. Lett.* **121**, 096401 (2018).
- [60] J.-X. Yin, S. S. Zhang, G. Chang, Q. Wang, S. S. Tsirkin, Z. Guguchia, B. Lian, H. Zhou, K. Jiang, I. Belopolski, N. Shumiya, D. Multer, M. Litskevich, T. A. Cochran, H. Lin, Z. Wang, T. Neupert, S. Jia, H. Lei, and M. Z. Hasan, Negative flat band magnetism in a spin-orbit-coupled correlated kagome magnet, *Nat. Phys.* **15**, 443 (2019).
- [61] M. Li, Q. Wang, G. Wang, Z. Yuan, W. Song, R. Lou, Z. Liu, Y. Huang, Z. Liu, H. Lei, Z. Yin, and S. Wang, Dirac cone, flat band and saddle point in kagome magnet  $\text{YMn}_6\text{Sn}_6$ , *Nat. Commun.* **12**, 3129 (2021).
- [62] B. C. Sales, J. Yan, W. R. Meier, A. D. Christianson, S. Okamoto, and M. A. McGuire, Electronic, magnetic, and thermodynamic properties of the kagome layer compound  $\text{FeSn}$ , *Phys. Rev. Materials* **3**, 114203 (2019).
- [63] W. R. Meier, M.-H. Du, S. Okamoto, N. Mohanta, A. F. May, M. A. McGuire, C. A. Bridges, G. D. Samolyuk, and B. C. Sales, Flat bands in the  $\text{CoSn}$ -type compounds, *Phys. Rev. B* **102**, 075148 (2020).
- [64] Z. Liu, M. Li, Q. Wang, G. Wang, C. Wen, K. Jiang, X. Lu, S. Yan, Y. Huang, D. Shen, J.-X. Yin, Z. Wang, Z. Yin, H. Lei, and S. Wang, Orbital-selective Dirac fermions and extremely flat bands in frustrated kagome-lattice metal  $\text{CoSn}$ , *Nat. Commun.* **11**, 4002 (2020).
- [65] H. Huang, L. Zheng, Z. Lin, X. Guo, S. Wang, S. Zhang, C. Zhang, Z. Sun, Z. Wang, H. Weng, L. Li, T. Wu, X. Chen, and C. Zeng, Flat-band-induced anomalous anisotropic charge transport and orbital magnetism in kagome metal  $\text{CoSn}$ , *Phys. Rev. Lett.* **128**, 096601 (2022).
- [66] M. Kang, S. Fang, L. Ye, H. C. Po, J. Denlinger, C. Jozwiak, A. Bostwick, E. Rotenberg, E. Kaxiras, J. G. Checkelsky, and R. Comin, Topological flat bands in frustrated kagome lattice  $\text{CoSn}$ , *Nat. Commun.* **11**, 4004 (2020).
- [67] M. Kang, L. Ye, S. Fang, J.-S. You, A. Levitan, M. Han, J. I. Facio, C. Jozwiak, A. Bostwick, E. Rotenberg, M. K. Chan, R. D. McDonald, D. Graf, K. Kaznatcheev, E. Vescovo, D. C. Bell, E. Kaxiras, J. van den Brink, M. Richter, M. Prasad Ghimire, J. G. Checkelsky, and R. Comin, Dirac fermions and flat bands in the ideal kagome metal  $\text{FeSn}$ , *Nat. Mater.* **19**, 163 (2020).
- [68] Z. Lin, C. Wang, P. Wang, S. Yi, L. Li, Q. Zhang, Y. Wang, Z. Wang, H. Huang, Y. Sun, Y. Huang, D. Shen, D. Feng, Z. Sun, J.-H. Cho, C. Zeng, and Z. Zhang, Dirac fermions in antiferromagnetic  $\text{FeSn}$  kagome lattices with combined space inversion and time-reversal symmetry, *Phys. Rev. B* **102**, 155103 (2020).
- [69] M. Han, H. Inoue, S. Fang, C. John, L. Ye, M. K. Chan, D. Graf, T. Suzuki, M. P. Ghimire, W. J. Cho, E. Kaxiras, and J. G. Checkelsky, Evidence of two-dimensional flat band at the surface of antiferromagnetic kagome metal  $\text{FeSn}$ , *Nat. Commun.* **12**, 5345 (2021).
- [70] B. C. Sales, W. R. Meier, A. F. May, J. Xing, J.-Q. Yan, S. Gao, Y. H. Liu, M. B. Stone, A. D. Christianson, Q. Zhang, and M. A. McGuire, Tuning the flat bands of the kagome metal  $\text{CoSn}$  with Fe, In, or Ni doping, *Phys. Rev. Materials* **5**, 044202 (2021).
- [71] Y. Xie, L. Chen, T. Chen, Q. Wang, Q. Yin, J. R. Stewart, M. B. Stone, L. L. Daemen, E. Feng, H. Cao, H. Lei, Z. Yin, A. H. MacDonald, and P. Dai, Spin excitations in metallic kagome lattice  $\text{FeSn}$  and  $\text{CoSn}$ , *Commun. Phys.* **4**, 240 (2021).
- [72] C. Zeng, P. R. C. Kent, M. Varela, M. Eisenbach, G. M. Stocks, M. Torija, J. Shen, and H. H. Weitering, Epitaxial stabilization of ferromagnetism in the nanophase of  $\text{FeGe}$ , *Phys. Rev. Lett.* **96**, 127201 (2006).
- [73] M. Kakihana, K. Nishimura, D. Aoki, A. Nakamura, M. Nakashima, Y. Amako, T. Takeuchi, T. Kida, T. Tahara, M. Hagiwara, H. Harima, M. Hedo, T. Nakama, and Y. Onuki, Electronic states of antiferromagnet  $\text{FeSn}$  and Pauli paramagnet  $\text{CoSn}$ , *J. Phys. Soc. Jpn.* **88**, 014705 (2019).
- [74] D. Khadka, T. R. Thapaliya, J. Wen, R. F. Need, and S. X. Huang, High quality epitaxial thin films and exchange bias of antiferromagnetic dirac semimetal  $\text{FeSn}$ , *Appl. Phys. Lett.* **117**, 032403 (2020).
- [75] A. Ptok, A. Kobińska, M. Sternik, J. Łażewski, P. T. Jochym, A. M. Oleś, S. Stankov, and P. Piekarczyk, Chiral phonons in the honeycomb sublattice of layered  $\text{CoSn}$ -like compounds, *Phys. Rev. B* **104**, 054305 (2021).
- [76] P. C. Canfield, T. Kong, U. S. Kaluarachchi, and N. H. Jo, Use of frit-disc crucibles for routine and exploratory solution growth of single crystalline samples, *Philos. Mag.* **96**, 84 (2016).
- [77] V. Petříček, M. Dušek, and L. Palatinus, Crystallographic computing system JANA2006: General features, *Zeitschrift für Kristallographie - Crystalline Materials* **229**, 345 (2014).
- [78] P. E. Blöchl, Projector augmented-wave method, *Phys. Rev. B* **50**, 17953 (1994).
- [79] G. Kresse and J. Hafner, Ab initio molecular-dynamics simulation of the liquid-metal-amorphous-semiconductor transition in germanium, *Phys. Rev. B* **49**, 14251 (1994).
- [80] G. Kresse and J. Furthmüller, Efficient iterative schemes for ab initio total-energy calculations using a plane-wave basis set, *Phys. Rev. B* **54**, 11169 (1996).
- [81] G. Kresse and D. Joubert, From ultrasoft pseudopotentials to the projector augmented-wave method, *Phys. Rev. B* **59**, 1758 (1999).
- [82] J. P. Perdew, K. Burke, and M. Ernzerhof, Generalized gradient approximation made simple, *Phys. Rev. Lett.* **77**, 3865 (1996).
- [83] H. J. Monkhorst and J. D. Pack, Special points for Brillouin-zone integrations, *Phys. Rev. B* **13**, 5188 (1976).
- [84] R. Pott, R. Schefzyk, D. Wohlleben, and A. Junod, Thermal expansion and specific heat of intermediate valent  $\text{YbCuAl}$ , *Z. Physik B - Condensed Matter* **44**, 17 (1981).
- [85] M. S. Kim, Y. Echizen, K. Umeo, S. Kobayashi, M. Sera, P. S. Salamakha, O. L. Sologub, T. Takabatake, X. Chen, T. Tayama, T. Sakakibara, M. H. Jung, and M. B. Maple, Low-temperature anomalies in magnetic, transport, and thermal properties of single-crystal  $\text{CeRhSn}$  with valence fluctuations, *Phys. Rev. B* **68**, 054416 (2003).
- [86] E. Morosan, S. Bud'ko, P. Canfield, M. Torikachvili, and

- A. Lacerda, Thermodynamic and transport properties of  $R\text{AgGe}$  ( $R = \text{Tb-Lu}$ ) single crystals, *J. Magn. Magn. Mater.* **277**, 298 (2004).
- [87] S. F. Matar, J. F. Riecken, B. Chevalier, R. Pöttgen, A. F. Al Alam, and V. Eyert, Electronic and magnetic properties and chemical bonding of  $\text{Ce}M\text{Sn}$  ( $M = \text{Rh, Ru}$ ) from first principles, *Phys. Rev. B* **76**, 174434 (2007).
- [88] F. R. de Boer, R. A. Elenbaas, and W. C. M. Mattens, Abstract: Mixed valence behaviour in the intermetallic compound  $\text{YbCuAl}$ , *J. Appl. Phys.* **49**, 2100 (2008).
- [89] Y. Qian, S. Nie, C. Yi, L. Kong, C. Fang, T. Qian, H. Ding, Y. Shi, Z. Wang, H. Weng, and Z. Fang, Topological electronic states in  $\text{HfRuP}$  family superconductors, *npj Comput. Mater.* **5**, 121 (2019).
- [90] H. Su, T. Shang, F. Du, C. F. Chen, H. Q. Ye, X. Lu, C. Cao, M. Smidman, and H. Q. Yuan,  $\text{NbReSi}$ : A non-centrosymmetric superconductor with large upper critical field, *Phys. Rev. Materials* **5**, 114802 (2021).
- [91] T. Asaba, V. Ivanov, S. M. Thomas, S. Y. Savrasov, J. D. Thompson, E. D. Bauer, and F. Ronning, Colossal anomalous Nernst effect in a correlated noncentrosymmetric kagome ferromagnet, *Sci. Adv.* **7**, eabf1467 (2021).
- [92] R. Kumar, S.-S. Luo, F. Du, H. Su, J. Zhang, C. Cao, and H. Q. Yuan, Superconductivity in non-centrosymmetric  $\text{ZrNiAl}$  and  $\text{HfRhSn}$ -type compounds, *J. Phys.: Condens. Matter* **34**, 435701 (2022).
- [93] Supplemental Material at [URL will be inserted by publisher] for more details of the crystallographic data, XRD refinements, and additional numerical results. This Supplemental Material contain Ref. [62–66, 70, 72–74, 114–116].
- [94] K. Parlinski, Z. Q. Li, and Y. Kawazoe, First-principles determination of the soft mode in cubic  $\text{ZrO}_2$ , *Phys. Rev. Lett.* **78**, 4063 (1997).
- [95] A. Togo and I. Tanaka, First principles phonon calculations in materials science, *Scripta Materialia* **108**, 1 (2015).
- [96] M. P. L. Sancho, J. M. L. Sancho, J. M. L. Sancho, and J. Rubio, Highly convergent schemes for the calculation of bulk and surface Green functions, *J. Phys. F: Met. Phys.* **15**, 851 (1985).
- [97] Q. S. Wu, S. N. Zhang, H.-F. Song, M. Troyer, and A. A. Soluyanov, WANNIERTOOLS: An open-source software package for novel topological materials, *Comput. Phys. Commun.* **224**, 405 (2018).
- [98] O. Hellman, I. A. Abrikosov, and S. I. Simak, Lattice dynamics of anharmonic solids from first principles, *Phys. Rev. B* **84**, 180301(R) (2011).
- [99] P. T. Jochym and J. Łażewski, High Efficiency Configuration Space Sampling – probing the distribution of available states, *SciPost Phys.* **10**, 129 (2021).
- [100] M. Sinha, H. K. Vivanco, C. Wan, M. A. Siegler, V. J. Stewart, E. A. Pogue, L. A. Pressley, T. Berry, Z. Wang, I. Johnson, M. Chen, T. T. Tran, W. A. Phelan, and T. M. McQueen, Twisting of 2D kagome sheets in layered intermetallics, *ACS Central Science* **7**, 1381 (2021).
- [101] J.-X. Yin, N. Shumiya, S. Mardanya, Q. Wang, S. S. Zhang, H.-J. Tien, D. Multer, Y. Jiang, G. Cheng, N. Yao, S. Wu, D. Wu, L. Deng, Z. Ye, R. He, G. Chang, Z. Liu, K. Jiang, Z. Wang, T. Neupert, A. Agarwal, T.-R. Chang, C.-W. Chu, H. Lei, and M. Z. Hasan, Fermion–boson many-body interplay in a frustrated kagome paramagnet, *Nat. Commun.* **11**, 4003 (2020).
- [102] L. Brey and H. A. Fertig, Electronic states of graphene nanoribbons studied with the Dirac equation, *Phys. Rev. B* **73**, 235411 (2006).
- [103] K. Wakabayashi, Y. Takane, and M. Sigrist, Perfectly conducting channel and universality crossover in disordered graphene nanoribbons, *Phys. Rev. Lett.* **99**, 036601 (2007).
- [104] W. Yao, S. A. Yang, and Q. Niu, Edge states in graphene: From gapped flat-band to gapless chiral modes, *Phys. Rev. Lett.* **102**, 096801 (2009).
- [105] B.-J. Yang and N. Nagaosa, Emergent topological phenomena in thin films of pyrochlore iridates, *Phys. Rev. Lett.* **112**, 246402 (2014).
- [106] Z. Li, J. Zhuang, L. Wang, H. Feng, Q. Gao, X. Xu, W. Hao, X. Wang, C. Zhang, K. Wu, S. X. Dou, L. Chen, Z. Hu, and Y. Du, Realization of flat band with possible nontrivial topology in electronic kagome lattice, *Science Advances* **4**, eaau4511 (2018).
- [107] A. Mook, J. Henk, and I. Mertig, Edge states in topological magnon insulators, *Phys. Rev. B* **90**, 024412 (2014).
- [108] D. Malz, J. Knolle, and A. Nunnenkamp, Topological magnon amplification, *Nat. Commun.* **10**, 3937 (2019).
- [109] H. Zhong, R. Wang, F. Ye, J. Zhang, L. Zhang, Y. Zhang, M. R. Belić, and Y. Zhang, Topological insulator properties of photonic kagome helical waveguide arrays, *Results in Physics* **12**, 996 (2019).
- [110] X. Xi, J. Ma, S. Wan, C.-H. Dong, and X. Sun, Observation of chiral edge states in gapped nanomechanical graphene, *Sci. Adv.* **7**, eabe1398 (2021).
- [111] S. Basak and A. Ptok, Theoretical study of dynamical and electronic properties of noncentrosymmetric superconductor  $\text{NbReSi}$ , *Materials* **16**, 78 (2023).
- [112] K. Momma and F. Izumi, VESTA3 for three-dimensional visualization of crystal, volumetric and morphology data, *J. Appl. Crystallogr.* **44**, 1272 (2011).
- [113] A. Kokalj, Xcrysden—a new program for displaying crystalline structures and electron densities, *J. Mol. Graph. Model.* **17**, 176 (1999).
- [114] M. Jovanovic and L. M. Schoop, Simple chemical rules for predicting band structures of kagome materials, *J. Am. Chem. Soc.* **144**, 10978 (2022).
- [115] F. Herman, C. D. Kuglin, K. F. Cuff, and R. L. Kortum, Relativistic corrections to the band structure of tetrahedrally bonded semiconductors, *Phys. Rev. Lett.* **11**, 541 (1963).
- [116] K. V. Shanavas, Z. S. Popović, and S. Satpathy, Theoretical model for Rashba spin-orbit interaction in  $d$  electrons, *Phys. Rev. B* **90**, 165108 (2014).

# Supplemental Material

## Phononic drumhead surface state in distorted kagome compound RhPb

Andrzej Ptok *et al.*

(Dated: September 6, 2023)

In this Supplemental Material, we present additional results:

- Table S1 – Crystallographic data obtained from x-ray diffraction.
- Table S2 – Atomic displacement parameters.
- **Section S1** – Section describing electronic band structure of RhPb with  $P6/mmm$  and  $P\bar{6}2m$  symmetries.
- Fig. S1 – Comparison of electronic band structure of RhPb with  $P6/mmm$  and  $P\bar{6}2m$  symmetries.
- Fig. S2 – Comparison of the electronic density of states for RhPb with  $P6/mmm$  and  $P\bar{6}2m$  symmetries.
- Fig. S3 – Fermi surface for RhPb with  $P\bar{6}2m$ .
- Fig. S4 – ARPES results for (001) surface.
- **Section S2** – Section discussing the phonon irreducible representation at  $\Gamma$  point of RhPb with  $P6/mmm$  and  $P\bar{6}2m$  symmetries.
- Table S3 – Characteristic frequencies and symmetries of the phonon modes at  $\Gamma$  point of RhPb with  $P6/mmm$  and  $P\bar{6}2m$  symmetries.

### S1. ELECTRONIC PROPERTIES

Typically, CoSn-like compounds, containing ideal kagome lattice of the  $d$ -block elements (i.e.,  $P6/mmm$  symmetry), are characterized by the electronic flat-bands [62–66]. Similarly, to the case of the phonon dispersion, the electronic band structure possesses several nearly-flat bands. The orbital character of the flat bands, with bands in range of around 0.5 eV, are associated with the combination of  $d_{xy}$  and  $d_{x^2-y^2}$ , or  $d_{xz}$  and  $d_{yz}$  orbitals [63]. In fact, the RhPb with  $P6/mmm$  symmetry exhibits the complex electronic band structure of the kagome lattice, as a consequence of the emergence of the isolated kagome net by Rh atoms [114]. In this case, the kagome-like band structure is formed in energies between  $-3$  and  $-1$  eV [see Fig. S1(a)]. The introduction of the distortion in the kagome lattice does not change this feature [see Fig. S1(b)].

TABLE S1. Refined RhPb structures from single crystal x-ray diffraction. Note that the  $P\bar{6}2m$  space group gives a better refinement.

		RhPb	
Chem formula	RhPb		
Formula wt. (g/mol.f.u.)	310.11		
Wavelength	Mo $K_\alpha$ (0.71073 Å)		
Temperature (K)	293(2)		
Symmetry	$P6/mmm$	$P\bar{6}2m$	
$Z$	3	3	
Calc. density (g/cm <sup>3</sup> )	12.4801	12.4801	
$a, b$ (Å)	5.6794(4)	5.6794(4)	
$c$ (Å)	4.4311(3)	4.4311(3)	
$V$ (Å <sup>3</sup> )	123.779(19)	12.779(19)	
$x_{Rh}$	1/2	0.4775(2)	
Twin fraction	N.A.	0.568(25)	
Rh hexagon angles (°)	120	128.91(4)	
		/111.09(4) <sup>a</sup>	
F(000)	381	381	
No. of reflections	163	264	
No. of observed reflections	160	259	
Refined based on $ F $			
Criteria for observed reflections	$I > 3s(I)'$	$I > 3s(I)'$	
Overall completeness			
Redundance index ranges			
$h$	-9 9	-9	9
$k$	-10 4	-10	4
$l$	-7 7	-7	7
No. of variables	10	12	
$N_{ref}/N_{var}$			
R(obs) (%)	6.01	2.83	
wR(obs) (%)	8.94	3.55	
R(all) (%)	6, 08	4.23	
wR(all) (%)	8.95	4.04	
Goodness of fit obs	4.91	1.65	
Goodness of fit all	4.86	1.86	
$\mu$	111.222	111.222	
Extinction coeff.	1700(400)	660(90)	

<sup>a</sup> Triangles rotated by  $4.45(3)^\circ$ .

Unlike the ferromagnetic FeGe [72] or antiferromagnetic FeSn [62, 70, 73, 74], RhPb does not exhibit magnetic order. The electronic band structure decoupling is introduced by the relatively strong spin-orbit coupling (cf. band structures in the absence and presence of the spin-orbit coupling, presented by the orange and blue lines, respectively, in Fig. S1). In practice, the strength of the spin-orbit coupling is strictly related to the atomic mass of the elements [115, 116]. Indeed, in our case, the relatively weak impact of the spin-orbit coupling is observed in the range energies related to the  $d$  orbitals of Rb, while stronger in the case of Pb atoms contribution. For example, the band splitting along the  $\Gamma$ -A path is in

TABLE S2. Atomic displacement parameters.

$P6/mmm$	$U_{11}$	$U_{22}$	$U_{33}$	$U_{12}$	$U_{13}$	$U_{23}$	$U_{iso}$
Pb	0.0096(6)	0.0096(6)	0.0058(9)	0.0048(3)	0	0	0.0084(5)
Pb	0.0137(7)	0.0137(7)	0.0167(12)	0.0068(4)	0	0	0.0147(6)
Rh	0.0256(12)	0.0047(9)	0.0082(13)	0.0024(5)	0	0	0.0152(8)
$P\bar{6}2m$	$U_{11}$	$U_{22}$	$U_{33}$	$U_{12}$	$U_{13}$	$U_{23}$	$U_{iso}$
Pb	0.0103(2)	0.0103(2)	0.0035(3)	0.00517(11)	0	0	0.00806(19)
Pb	0.0092(3)	0.0092(3)	0.0157(5)	0.00462(13)	0	0	0.0114(2)
Rh	0.0105(4)	0.0069(4)	0.0063(5)	0.00345(19)	0	0	0.0083(3)

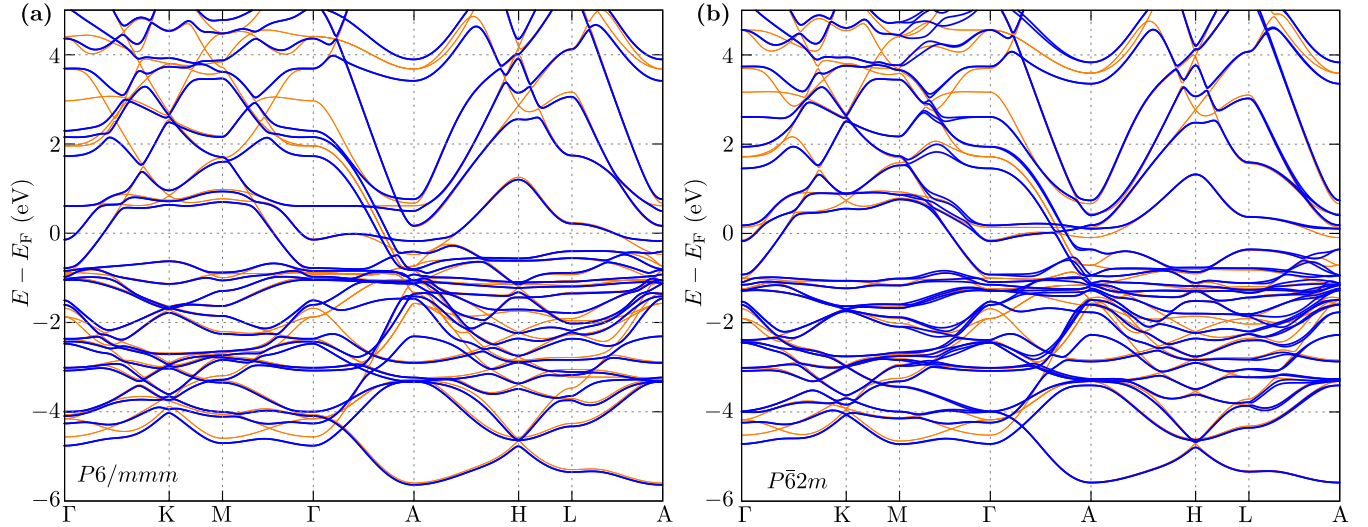


FIG. S1. Electronic band structure of RhPb for  $P6/mmm$  (a) and  $P\bar{6}2m$  (b) symmetry. Results in the presence (absence) of the spin-orbit coupling, are shown by a blue (orange) line.

the range 0.75 eV (cf. orange and blue lines in Fig. S1). Bigger splinting can also be observed above the Fermi level.

The Fermi surface contains three pockets (Fig. S3). The double-umbrella-like pocket is related to the electronic branch, which exhibits strong dispersion in the  $x$ - $y$

plane and weak along the  $z$  direction, while the ellipsoid pocket exhibits exact 3D electronic behavior. Similarly, the flat face of two pockets is related to the dispersionless branches in plane  $x$ - $y$ , but relatively strong electronic  $k_z$ -dependence dispersion. This feature is also reflected in the electronic band structure in the form of a parabolic-like band along  $\Gamma$ -A path (see Fig. S1).

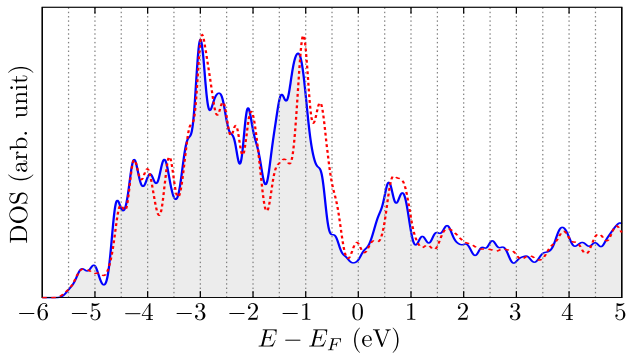


FIG. S2. Comparison of the electronic density of states of RhPb with  $P6/mmm$  and  $P\bar{6}2m$  symmetries (red and blue lines, respectively).

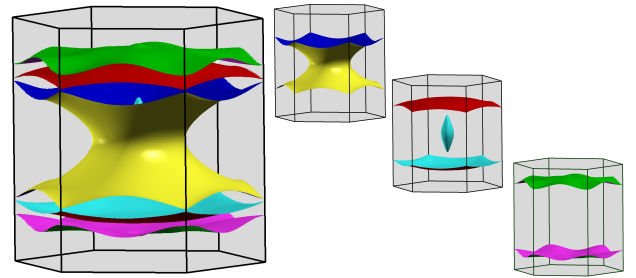


FIG. S3. The Fermi surface of RhPb for  $P\bar{6}2m$ . The big panel represents the total Fermi surface, while the small panels present the separate Fermi pockets formed by separate bands.

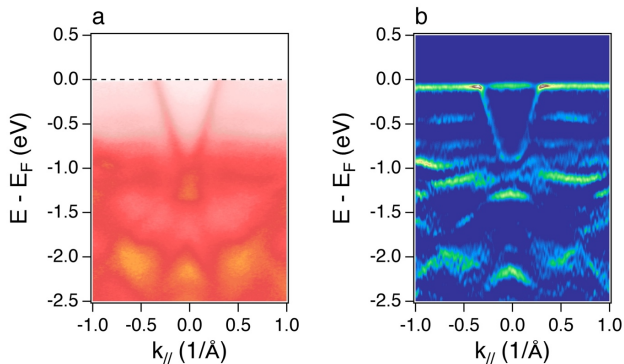


FIG. S4. ARPES result for (001) surface along the K- $\Gamma$ -K direction. ARPES intensity plot (a) and the second derivative of the intensity (b). The data was collected at incident photon energy  $h\nu = 70$  eV, corresponding to  $k_z = \pi$ .

### A. APRES spectra

The ARPES experiment was carried out on beamline 21-ID-1 at the National Synchrotron Light Source II, Brookhaven. All samples were cleaved in situ under vacuum better than  $5 \times 10^{-11}$  Torr. Measurements were taken with a synchrotron light source and a Scienta-Omicron DA30 electron analyzer. The total energy resolution was set to 15 meV. The sample stage was maintained at low temperature ( $T = 15$  K) throughout the experiment.

Results of ARPES measurements are presented in Fig. S4. Multiple flat-like bands are observed near the binding energy 1 eV, consistent with DFT calculations presented in Fig. S1. Near the Fermi level, only one parabolic electron-like band is observed at the  $\Gamma$  point.

### S2. ACTIVE MODES

In the case of  $P6/mmm$  symmetry, the phonon modes at the  $\Gamma$  point can be decomposed into irreducible repre-

sentation as follows:

$$\begin{aligned} \Gamma_{\text{acoustic}} &= A_{2u} + E_{1u}, \\ \Gamma_{\text{optic}} &= 2A_{2u} + B_{1g} + B_{1u} + B_{2u} \\ &\quad + E_{2u} + E_{2g} + 3E_{1u}, \end{aligned} \quad (\text{S1})$$

where  $2A_{2u} + 3E_{1u}$  (acoustic modes not included) are infrared (IR) active, while  $E_{2g}$  mode (with frequency 3.275 THz) is Raman active. IR active modes are related to the vibration of all atoms in the structure, while Raman active mode only with vibration of atoms in the Wyckoff  $2d$  position (i.e., Pb atoms forming honeycomb lattice). Similarly, in the case  $P\bar{6}2m$  we get:

$$\begin{aligned} \Gamma_{\text{acoustic}} &= A_2'' + E', \\ \Gamma_{\text{optic}} &= A_1' + A_2' + A_1'' + 2A_2'' + 4E' + E'', \end{aligned} \quad (\text{S2})$$

where  $2A_2'' + 4E'$  modes are IR active, while  $A_1' + 4E' + E''$  modes are Raman active. In the case of this symmetry, both IR and Raman active modes are related to vibrations of all atoms. Additionally, as we can see, more modes are active in the case of  $P\bar{6}2m$  than in  $P6/mmm$  symmetry, which could be an additional way to confirm the realized phase. Nevertheless, the degeneracy of the bands at the  $\Gamma$  point is the same in both phases. Characteristic frequencies and their symmetries can be found in Tab. S3.

TABLE S3. Characteristic frequencies (THz) and symmetries of the phonon modes at the  $\Gamma$  point for RhPb with both symmetries.

$P6/mmm$							
-2.590	( $B_{1u}$ )	0.000	( $A_{2u}$ )	0.000	( $E_{1u}$ )	1.675	( $A_{2u}$ )
2.119	( $E_{1u}$ )	2.519	( $E_{1u}$ )	3.260	( $E_{1u}$ )	3.275	( $E_{2g}$ )
3.754	( $B_{1g}$ )	5.267	( $A_{2u}$ )	5.355	( $E_{1u}$ )	6.296	( $B_{2u}$ )
$P\bar{6}2m$							
0.000	( $A$ )	0.000	( $E$ )	1.777	( $A$ )	2.160	( $E$ )
2.886	( $E$ )	3.291	( $E$ )	3.296	( $A$ )	3.689	( $E$ )
3.737	( $A$ )	5.273	( $A$ )	5.507	( $E$ )	6.066	( $A$ )